Journal of Wind Engineering & Industrial Aerodynamics 256 (2025) 105950

Contents lists available at ScienceDirect

Journal of Wind Engineering & Industrial Aerodynamics

journal homepage: www.elsevier.com/locate/jweia

A predictive large-eddy simulation framework for the analysis of wind loads on a realistic low-rise building geometry

Themistoklis Vargiemezis *, Catherine Gorlé

Stanford University, Y2E2 Building, 473 Via Ortega, Stanford, CA, 94305, United States of America

ARTICLE INFO

Keywords:
Large-eddy simulation
Framework
Wind-tunnel
Low-rise building
Pressure loads

ABSTRACT

The accuracy of large-eddy simulations (LESs) for predicting wind-induced pressure loads remains an important topic of inquiry. This paper aims to advance this topic by validating an LES workflow for predicting wind pressures on a realistic low-rise building model exposed to a suburban neutral surface layer. We compare two wind tunnel data sets and LES predictions, obtained using a two-step workflow. First, we ensure that an accurate representation of the surface layer wind flow is obtained at the building location. Next, we assess the resulting wind loads on the building model. Using this workflow, we demonstrate consistent agreement between LES predictions and wind tunnel tests, where the discrepancies between the LES and wind tunnel results mimic the discrepancies between the two wind tunnel tests. This finding underscores that the pressure signals in certain locations are sensitive to inevitable, small differences in the approach flow. LES-based flow visualization uncovered that the most negative pressure peaks, which occur on the building roof, arise from hairpin-like vortices that are lifted from the separation region near the upstream roof edge. The results shed light on the complex dynamics of wind-induced pressure loads and contribute to quantifying the reliability of LES for wind load estimation.

1. Introduction

Extreme wind events can cause significant wind-induced damage to buildings and their components. In a comprehensive recent evaluation, it was revealed that the United States experienced 20 confirmed wind-induced disasters in the year 2023 alone (Smith, 2023). The cost for each of these disaster events is estimated to exceed $1 billion. Since the majority of structures worldwide are low-rise buildings, accurate prediction of wind loads on these buildings is essential to support wind-resistant design and improve community resilience to extreme wind events.

The analysis of wind loads on low-rise buildings typically relies on building codes and standards. These standards are based on extensive databases obtained from wind tunnel measurements that have been performed to define design pressure coefficients (Holmes, 1983; Stathopoulos, 1984; Kasperski, 1996; Alrawashdeh and Stathopoulos, 2015; ASCE, 2022). However, the assessment of wind loads based on codes and standards inevitably requires simplifications and assumptions that can affect accuracy. It is particularly challenging to accurately represent the effect of non-standard geometrical features, such as non-standard building shapes, locally complex terrain, surrounding buildings, or geometrical details in the design. For example, a recent experimental study showed that the wind pressures acting on roofs of L- and T-shaped low-rise buildings differ considerably from those encountered by regular rectangular buildings (Shao et al., 2018). Wind tunnel testing of a specific low-rise building design could more accurately represent the effect of geometrical details, but the availability and high cost of operation of atmospheric boundary layer wind tunnels, as well as geometrical scaling challenges, are limiting factors.

Computational Fluid Dynamics (CFD) simulations, in particular large-eddy simulations (LESs), offer an alternative strategy for evaluating wind loads on low-rise buildings. LESs resolve the large-scale turbulent structures in the flow, allowing for accurate simulations of the complex phenomena that govern peak wind loads, such as flow separation and vortex shedding (Ricci et al., 2017; Blocken, 2014; Geleta and Bitsuamlak, 2022; Richards and Norris, 2015). The simulations can represent the effect of local geometrical features to provide more accurate assessments of wind loads on specific buildings. Furthermore, CFD could support the generation of extensive new databases to update and improve the accuracy of building codes and standards for the calculation of wind loads on low-rise buildings. Previous studies have successfully demonstrated the effectiveness of LES for calculating wind loads on idealized low-rise buildings with rectangular floorplans (Ricci et al., 2017; Geleta and Bitsuamlak, 2022). However, the potential

---

* Corresponding author.
E-mail addresses: tvarg@stanford.edu (T. Vargiemezis), gorle@stanford.edu (C. Gorlé).

https://doi.org/10.1016/j.jweia.2024.105950
Received 2 April 2024; Received in revised form 8 October 2024; Accepted 4 November 2024

sensitivity of LES to model choices and the lack of validation on more complex geometries should be addressed for CFD to become widely accepted as an alternative design tool for the assessment of wind loads on buildings (Alrawashdeh and Stathopoulos, 2015).

The objective of this paper is to validate an LES workflow for predicting wind loading on a realistic low-rise building geometry. The test case considered is the Yang and Yamazaki Environment and Energy (Y2E2) building, located on the Stanford engineering quad (SEQ). The building has an L-shaped floorplan and includes covered walkways, terraces, and roof equipment. Validation data was obtained from experiments performed at two wind tunnels; the Natural Hazards Engineering Research Infrastructure (NHERI) Wall of Wind (WOW) wind tunnel at Florida International University facility (Gan Chowdhury et al., 2017), and the NHERI terraformer Boundary Layer Wind Tunnel at the University of Florida (UF) (Catarelli et al., 2020). Both wind tunnel tests and LES consider the 1:100 scaled model. The workflow consists of a two-step process that has previously been used for validation of wind loading predictions on high-rise buildings (Lamberti and Gorlé, 2020; Ciarlatani et al., 2023). First, LES simulations of a domain without the Y2E2 building are performed to ensure that the undisturbed flow conditions at the building location match the conditions on the wind tunnel turntable in terms of the mean velocity, turbulence intensities, and turbulence length scales. We will show that this step requires special care when considering low-rise buildings that are entirely embedded in the roughness sublayer. Second, the building is included in the domain to obtain predictions of the mean, root-mean-square, and peak wind pressure coefficients along the building façades and roof. These predictions are compared to the wind tunnel measurement data to enable a comprehensive assessment of LES as a tool for calculating wind loads on low-rise buildings. Lastly, the LES solution will be used to identify the flow physics that generate peak suction loads.

The paper is organized as follows. Section 2 provides an overview of the experimental setup for collecting data for the relevant quantities of interest. Section 3 outlines the LES setup and the methodology to calculate the relevant pressure statistics. Then, Section 4 analyses the results obtained from the LES and presents the comparison to the wind tunnel data. Finally, Section 5 summarizes the key findings and conclusions of the study.

2. Wind tunnel measurements

This section describes the experiments conducted in two wind tunnels. The first set of tests was performed in the WoW facility. This facility is a large-scale open-jet wind tunnel with a 6.1 m wide and 4.3 m high test section that includes a 4.9 m diameter turntable. The second set of tests was performed in the UF boundary layer wind tunnel, which is an open circuit low-speed tunnel with a test section measuring 6 m in width and 3 m in height, and a 1-meter diameter turntable. The goal of performing two sets of tests was to determine the reproducibility of the pressure measurements between two different experimental facilities. Both tests were conducted with a comparable suburban terrain configuration and considered 28 wind directions.

The following section provides a detailed description of the velocity measurements performed to characterize the boundary layer velocity statistics at the center of the turntable in the absence of the model. These velocity measurements are crucial to ensure that similar conditions are achieved in both wind tunnels and that they can be reproduced in the LESs. Subsequently, the discussion focuses on the setup employed for the pressure measurements on the low-rise building. The last subsection summarizes the quantities of interest for both the velocity and pressure measurements.

Table 1
Sampling frequency, total duration, and reference velocity at 0.2 m reference height for the velocity measurements performed in both facilities.

Facility	f_{samp} [Hz]	T [s]	U_{ref} [m/s]
WoW	2500	180	15.2
UF	850	180	11.8

2.1. Atmospheric boundary layer and reference velocity characterization

The generation of representative atmospheric boundary layer (ABL) wind conditions requires special consideration when performing measurements on low-rise buildings. These buildings are characterized by a low Jensen number, $\mathcal{O}(10)$, which is defined as the ratio of building height, H, to the roughness height, z_0. This characteristic can make low-rise buildings more difficult to model than high-rise buildings because the buildings are embedded in the roughness sublayer and the resulting wind pressures will be more strongly influenced by the presence of the upstream roughness elements. Hence, to maintain realistic ABL velocity statistics at the building location on the turntable, the roughness elements are extended beyond the upstream flow development section onto the turntable.

Fig. 1 shows the resulting setup to generate and measure the ABL in the WoW (left) and the UF ABL wind tunnel (center). The discrete points at which the time series of the three velocity components were measured using cobra probes are shown on the right in Fig. 1. In the WoW wind tunnel, the three velocity components (u, v, w) were measured with a sampling frequency of 2500 Hz at 35 distinct locations on a vertical plane at the center of the turntable. The probes covered seven elevations and five positions along the span, as illustrated in Fig. 1. The points were uniformly spaced at 0.04 m and 0.5 m intervals in the vertical (y) and horizontal (z) directions, respectively. These measurements support capturing the boundary layer profiles as a function of height, as well as identifying any variation in the profiles in the spanwise direction. In the UF wind tunnel, twelve probes were positioned at a single spanwise location at the center of the turntable. The probes were spaced at vertical intervals of approximately 0.05 m, covering a height from 0.05 m to 0.55 m, as depicted in Fig. 1. The sampling frequency of the measurements was 850 Hz. Table 1 summarizes the parameters of the WoW and UF experiments in terms of sampling frequency and total duration.

Table 1 also reports the reference velocity, which was measured using three additional cobra probes positioned 4 m upstream of the center of the turntable at building roof height (0.2 m), with a spanwise spacing of 0.5 m. These locations are indicated in Fig. 2 using yellow circles. These probes are also used to determine the reference velocity for calculating the pressure coefficients from the pressure measurements. In the WoW, the recorded values and the spanwise variability at the upstream location matched the values and variability measured at the turntable center. Hence, the recorded upstream values were used directly as the reference velocity. In the UF tunnel, the ABL measurements indicated that the boundary layer continued to develop between the upstream location and the center of the turntable, with a difference of 1 m/s in the upstream reference velocity compared to the turntable velocity at the same height. Hence, the reference velocity used to calculate the pressure coefficients is obtained by taking the recorded upstream values and adding this discrepancy.

2.2. Building model and pressure measurements

The building model, shown in Fig. 3, is a 1:100 scale model of the Y2E2 building located on Stanford's Engineering Quad. The model dimensions are 1 m long, 0.64 m wide, and 0.21 m high. The model has a relatively high level of detail in the geometry, including overhangs, pillars, and the rooftop atria and equipment. Fig. 3 includes the names

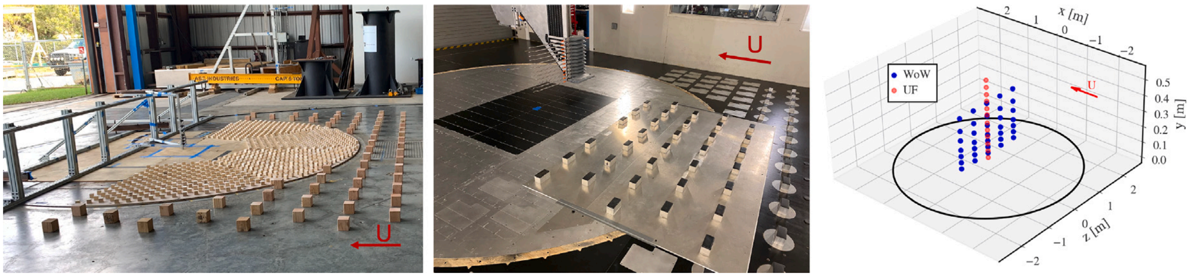

Fig. 1. ABL generation and measurement setup at WoW (left) and UF (middle), and a sketch of the cobra probes locations (right).

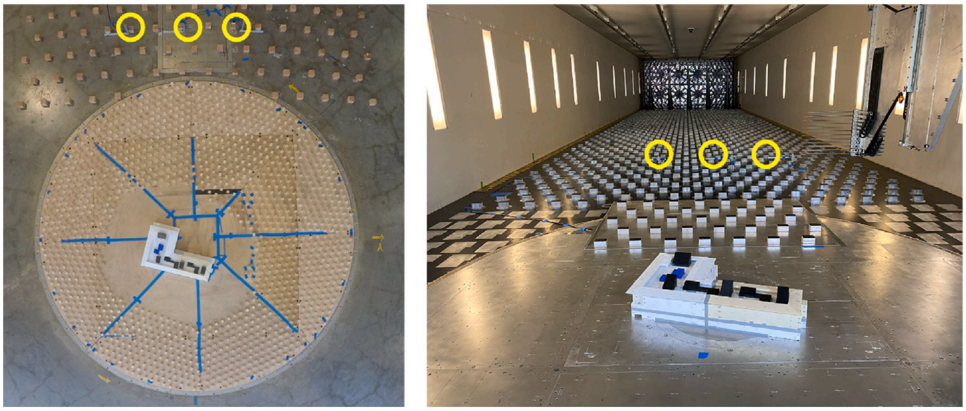

Fig. 2. Cobra probes locations for reference velocity measurements in WoW (left) and UF (right) wind tunnels.

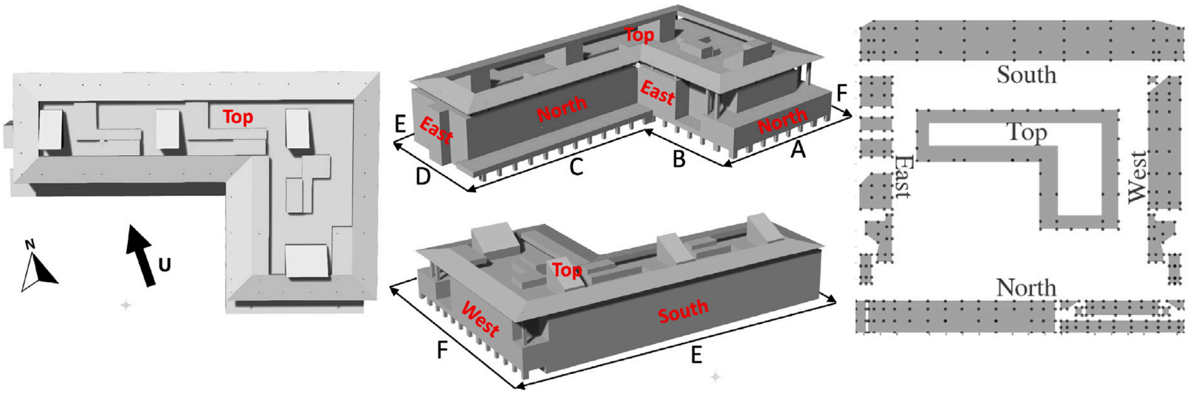

Fig. 3. Top view (left), 3D perspectives (center), and tap distribution on the Y2E2 model (right). Arrow shows the dominant wind direction.

Table 2
Sampling frequency, total duration, and reference velocity at 0.2 m reference height for the pressure measurements performed in both facilities.

Facility	f_{samp} [Hz]	T [s]	U_{ref} [m/s]
WoW	520	120	15.2
UF	620	180	11.8

for each face on the building and the arrow shows the dominant wind direction at the site, which is 1.8° with respect to the North.

The building is instrumented with 382 pressure taps placed along the exterior surface, as shown in Fig. 3. The pressure taps were connected with tubing to a Scanivalve ZOC33 analog scanner. Table 2 summarizes the sampling frequency, total duration, and reference velocity at 0.2 m height for the pressure measurements in both facilities.

Measurements were performed across a total of 28 wind directions, encompassing the complete wind rose. The full dataset is available in Vargiemezis and Gorle (2024). The analysis in this paper focuses primarily on the dominant wind direction.

2.3. Quantities of interest

2.3.1. Velocity statistics

Detailed knowledge of the incoming ABL velocity statistics plays a pivotal role in the validation process for LES of wind pressures on buildings. In addition to measuring the mean velocity profile U as a function of height, the statistics of the three turbulent velocity components, u', v' and w', should also be carefully documented. These statistics include the three turbulent intensities I_u, I_v, and I_w, which are calculated by dividing the square-root of the respective velocity variances by the mean streamwise velocity, U, measured at the same height:

$$I_u = \frac{\sqrt{\overline{u'^2}}}{U} \quad ; \quad I_v = \frac{\sqrt{\overline{v'^2}}}{U} \quad ; \quad I_w = \frac{\sqrt{\overline{w'^2}}}{U}. \tag{1}$$

Furthermore, information on the turbulent time and length scales has to be obtained. First, the integral time scales for the three velocity components, T_u, T_v, and T_w, are estimated by approximating the normalized auto-correlation function of the respective velocity signals with an exponential decay function: $R_\tau = exp(-\tau/T)$. Then, the time scale corresponds to the value for τ at which $R_\tau = exp(-1)$. Next, the three streamwise integral length scales are estimated using Taylor's frozen turbulent hypothesis, which transforms integral time scales into length scales. Each velocity component's streamwise length scale is then determined as:

$$L_{u,x} = T_u \times U \quad ; \quad L_{v,x} = T_v \times U \quad ; \quad L_{w,x} = T_w \times U. \tag{2}$$

2.3.2. Pressure statistics

For the pressure measurements the quantities of interest (QoIs) are the statistics of the time series of the non-dimensional pressure coefficient, defined as follows:

$$C_p(t) = \frac{p(t) - P_{\text{ref}}}{\frac{1}{2}\rho U_{ref}^2} \tag{3}$$

where p is the instantaneous pressure, P_{ref} is the reference pressure recorded outside the test section in the WoW and in a chamber under the turntable at UF, ρ is the density of the air, and U_{ref} is the reference velocity at roof height. The effect of the spanwise variability in the ABL generated in the WoW and UF facilities is reflected by calculating the pressure coefficients using a minimum, maximum, and average velocity, as recorded by the three upstream cobra probes. This approach results in a minimum, average, and maximum estimate for all pressure coefficient statistics.

The statistics considered are the first 4 moments of the time series, i.e. C_p^{mean}, C_p^{rms}, C_p^{skew} and C_p^{kurt}. For C_p^{kurt} we present the values for the excess kurtosis, which is equal to 0 for a normal distribution. The skewness and kurtosis characterize the asymmetry and the heaviness of the tails of the distribution, which affect the expected peak values for the pressure.

In addition, the peak pressure coefficient C_p^{peak} is calculated using the Cook and Mayne method (Cook and Mayne, 1980), which estimates the peak values relative to a 22% probability of exceedance. The peak estimates are obtained by dividing the time series of C_p into 10-second windows, extracting the most negative peak from each window, and fitting a Gumbel distribution to the extreme values.

3. Large eddy simulations

Employing LES for investigating pressure loads on buildings entails a two-step workflow. First, an empty domain simulation is performed to ensure that the inflow conditions produce the target ABL velocity statistics at the building location. Subsequently, the building is positioned within the domain to capture and analyze pressure statistics. In this section, we first provide an overview of the LES solver. The two subsequent subsections discuss the specifics of the simulations performed for each step in the workflow.

3.1. Solver and numerics

The LESs in this study were conducted utilizing the low-Mach formulation of the CharLES code, developed by Cadence Design Systems. CharLES is a finite volume solver with an automated body-fitted meshing technique based on 3D-clipped Voronoi diagrams. This approach results in isotropic, polyhedral-type cells, proving highly effective for the high-fidelity simulation of turbulent flows. The solver has found successful application in various wind engineering problems, including the modeling of natural ventilation in both isolated buildings and buildings within complex urban environments (Hwang and Gorlé, 2022, 2023), and the assessment of wind loading on a high-rise building (Ciarlatani et al., 2023).

The low-Mach formulation of CharLES solves the filtered equations for conservation of mass and momentum with the density approximated as the sum of a background density and an isentropic, acoustic perturbation. The equations are given by:

$$\frac{\partial \tilde{\rho}}{\partial t} + \frac{\partial \tilde{\rho}\tilde{u}_j}{\partial x_j} = 0, \tag{4}$$

$$\frac{\partial \tilde{\rho}\tilde{u}_i}{\partial t} + \frac{\partial \tilde{\rho}\tilde{u}_i\tilde{u}_j}{\partial x_j} = -\frac{\partial \tilde{p}}{\partial x_i} + \frac{\tilde{\sigma}_{ij}}{\partial x_j}, \tag{5}$$

$$\tilde{\rho} = \frac{1}{c^2}(\tilde{p} - p_{\text{ref}}) + \rho_{\text{ref}}. \tag{6}$$

$\widetilde{(\cdot)}$ denotes the LES filtered quantities, $\tilde{\rho}$ is the density, δ is the Kronecker delta, c is the speed of sound, ρ_{ref} is the reference density, p_{ref} is the reference pressure, and $\tilde{\sigma}_{ij}$ is the stress tensor. The unresolved portion of the stress tensor is modeled using the Vreman subgrid model (Vreman, 2004).

The solver uses a second-order backward difference scheme in time and a second-order central discretization in space. The definition of a finite speed of sound results in a lower condition number for the pressure system of equations, which is now a Helmholtz equation instead of the Poisson equation that arises in fully incompressible formulations. In the zero Mach number limit, the system will discretely recover an incompressible formulation. Additional insights into the derivation of the Helmholtz system can be found in Ambo et al. (2020).

3.2. Simulation set-up to reproduce the WT ABL

The computational set-up for the empty domain simulations was designed to reproduce the WoW experiments and match the measured ABL statistics at the building location. In the following, we first provide details on the computational domain, the mesh, and the boundary conditions. Subsequently, we discuss the optimization of the inflow condition to achieve an accurate representation of the ABL.

3.2.1. Computational domain, boundary conditions, and mesh

The computational domain is $50H_{ref}$ long, $30H_{ref}$ wide, and $20H_{ref}$ high, where $H_{ref} = 0.2$ m is the roof height. The same domain size is used for the simulations with the isolated building, and the dimensions were defined to be sufficiently large to avoid any blockage effects and reproduce the conditions in the wind tunnels as closely as possible (Franke et al., 2011).

At the inflow boundary a turbulent velocity field is generated using the divergence-free digital filter method proposed by Kim et al. (2013). The details of the inflow condition and the optimization performed to achieve a representative flow at the future building location will be provided in Section 4.1. The two lateral boundaries are periodic, and a slip condition is applied at the top boundary. The outlet boundary condition is specified as a zero gradient condition. At the ground boundary, a rough wall function for a neutral ABL with a fixed roughness length of 0.0027 m is specified.

In previous simulations of high-rise buildings, the above set of boundary conditions was successfully used to optimize the inflow conditions and achieve representative velocity statistics over the building height (Ciarlatani et al., 2023). However, as mentioned in Section 2.1, low-rise buildings can be more challenging because of their low Jenssen number, and the combination of the rough wall function and optimized inflow condition was insufficient to sustain the target turbulence content over the building height. Therefore, similar to the approach of extending the roughness elements onto the turntable in the experiments, a simulation domain that explicitly models 10 rows of roughness elements upstream of the low-rise buildings was also considered. The roughness elements correspond to those used in the WoW experiments, which are 3.81 cm cubes with 12.7 cm spacing and are placed 4.5 m from the inlet of the computational domain. The distance between the future building location and the roughness elements is $3.4\times H_{ref}$, which

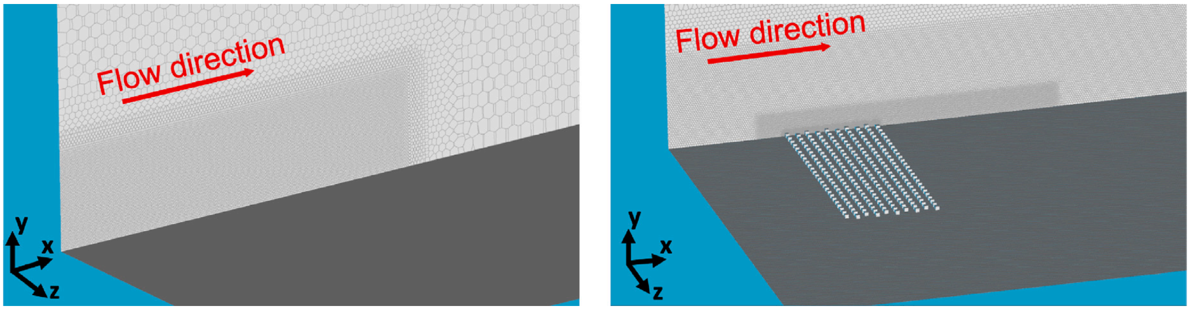

Fig. 4. Empty computational domains for the ABL simulations with an indicative grid resolution shown on a plane across the middle of the domain; left: ground boundary with a rough wall function applied (*WF*); right: rough wall function applied on the ground and 10 rows of roughness elements modeled (*WF+RE*).

Table 3
Grid resolution set-ups for the ABL grid convergence study.

Cases	Coarse	Baseline	Fine
Background cell size [mm]	100	100	100
ABL smallest cell size [mm]	25.0	12.5	6.2
Total number of cells for *LES WF* [millions of cells]	3.2	4.6	5.9
Total number of cells for *LES WF+RE* [millions of cells]	3.7	5.1	6.4

is the same as the two wind tunnel experiments. Fig. 4 shows both computational set-ups, which will be referred to as *WF* and *WF+RE* in the remainder of the paper.

The computational mesh used in the domain, with and without the elements, consists of Voronoi cells and was generated using the CharLES mesh generator. A grid sensitivity study was conducted using three different grid resolutions, as shown in Table 3. The grids only differ in terms of the grid size downstream of the roughness elements, where the building will be placed. The grid resolution around the roughness elements results in approximately 6 elements per roughness element height and is constant at the different grid resolutions tested. No significant difference was observed between the baseline and fine cases. As a result, the baseline case was chosen for the inflow optimization. It is important to note that the same setup, in terms of refinement boxes and background mesh size, was utilized for the simulations with the isolated building to ensure consistent length scales and turbulent intensities.

3.2.2. *Inflow boundary condition optimization*

The inflow boundary condition prescribes a logarithmic mean velocity profile at the inlet of the domain:

$$U = \frac{u^*}{\kappa} \ln\left(\frac{y + y_0}{y_0}\right), \tag{7}$$

where u^* is the friction velocity, κ is the von Kármán constant (0.41), and y_0 is the roughness length. Fitting the experimental data to this profile resulted in $u^* = 1.08$ m/s and $y_0 = 0.0027$ m. The corresponding Reynolds number is 2×10^5, based on the building roof height and the velocity at roof height.

To generate a turbulent velocity signal to be added to the mean velocity field, a divergence-free version of a digital filter developed by (Kim et al., 2013) is used. The method creates a synthetic turbulent field with user-defined Reynolds stress profiles, streamwise turbulent time scales for each velocity component, and spanwise and vertical length scales for each velocity component. The digital filter is used in combination with an acoustic subgrid scale sponge. The sponge is applied in a region that extends approximately two turbulent length scales downstream from the inlet, and damps high amplitude, short wavelength acoustic pressure fluctuations that are artificially introduced by the digital filtering turbulence generation.

Because of the synthetic nature of the turbulence, the turbulence statistics created by the digital filter method are known to decay further downstream in the computational domain, potentially resulting in considerably lower turbulent intensities and different lengthscales at the downstream location of interest. A straightforward procedure to resolve this issue is to employ the gradient-based optimization technique proposed by Lamberti et al. (2018), where the Reynolds stress profiles and time and length scales at the inflow are optimized to obtain the desired profiles at the building location.

Table 4
Lengthscales at 0.2 m reference height for the WoW and the optimized LES inflow.

Scales	T_u [s]	T_v [s]	T_w [s]	$L_{v,x}$ [m]	$L_{w,x}$ [m]
WoW	0.0448	0.0058	0.0151	0.0885	0.2291
LES inflow	0.0357	0.0062	0.0147	0.0942	0.2234

The optimization was initially performed for the empty domain simulations without roughness elements. This process could identify inflow conditions that result in a good representation of the target flow characteristics above the building roof height, but the turbulence intensities below the building roof height remained too low. When adding the roughness elements and using the optimized profiles the turbulence below building height reached adequate values. Section 4.1 will present a detailed comparison of the resulting velocity statistics at the building location to the target conditions.

Fig. 5 presents the target conditions at the building location together with the optimized inflow conditions used for the simulations presented in this paper. Table 4 summarizes the input for the time and length scales. The inflow generator requires as input the three time scales, T_u, T_v, and T_w and two length scales $L_{v,x}$, and $L_{w,x}$. The other length scales are approximated as follows:

$$L_{v,x} = L_{v,y} = L_{v,z} \quad ; \quad L_{w,x} = L_{w,y} = L_{w,z}, \tag{8}$$

and the $L_{u,x}$, $L_{u,y}$, and $L_{u,z}$, using the Taylor's frozen turbulent hypothesis, Eq. (2). It is emphasized that the optimized profiles and length scale values can only be expected to give the correct flow at the building location when using the same LES model set-up. Any studies aiming to model this test case using a different LES solver, subgrid model, or grid resolution, should perform a separate optimization to ensure the reported target profiles are matched at the building location.

3.3. *Simulation set-up with the building*

Once the inflow conditions are optimized and the desired profiles are obtained at the building location, the isolated building is imported inside the computational domain as shown in Fig. 6. All simulation settings, i.e. the domain size, the boundary conditions and the background mesh size are kept identical to the empty domain simulations.

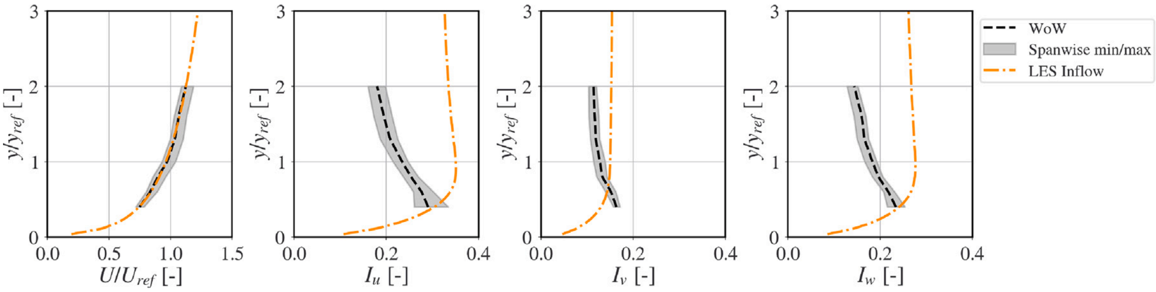

Fig. 5. Target mean velocity and turbulence intensity profiles at the building location and optimized profiles used for the inflow boundary condition in the simulations.

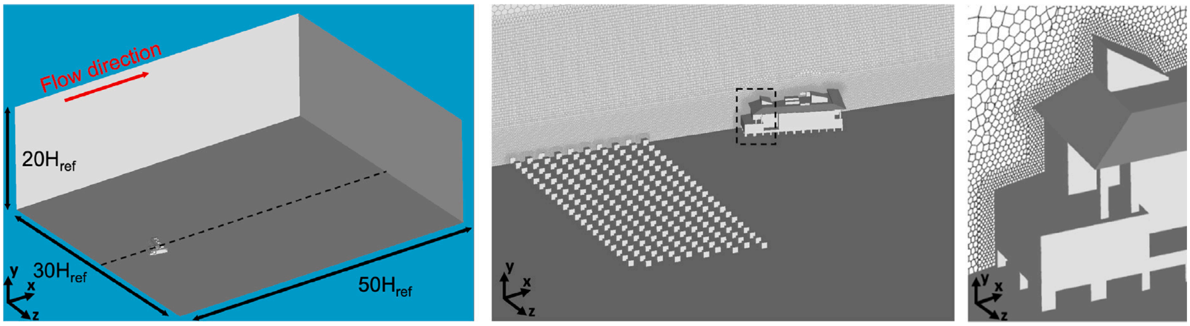

Fig. 6. Computational domain with the building. Left: domain dimensions, middle: zoom in on the building with a plane showing the grid refinements across the middle of the domain, and right: zoom in on the building surface. The plane in the middle figure is shown with the dashed line in the left figure, and the dashed box shows the building surface.

Table 5
Grid resolution set-ups for the grid convergence study with the building.

Cases	Coarse	Baseline	Fine
Building smallest cell size [mm]	6.2	3.1	1.6
Ratio of smallest cell size over H_{ref} [-]	0.030	0.015	0.007
Total number of cells with building [millions of cells]	5.1	6.8	9.7

The computational grid is generated using the CharLES mesh generator. A grid sensitivity study was conducted with the rough isolated case to determine the influence of the grid resolution on the pressure QoIs for the most dominant wind direction. Three different grid resolutions were considered, i.e., coarse, baseline, and fine. These meshes vary solely in terms of grid size around the building, while the placement, size, and number of transition layers in the refinement boxes away from the building surface remain consistent. The purpose of this approach is to ensure that the ABL statistics remain the same as those obtained in the empty domain ABL simulations. The background cell size, the smallest cell size, and the total number of cells are given in Table 5. Refinement boxes are placed around the roughness elements and the building in order to encompass the generated turbulence from the roughness elements, and the building wake region downstream. The mesh undergoes a gradual coarsening as it extends away from the building. This coarsening process involves doubling the cell size every 5 layers of cells until the background cell size is attained. Subsequently, this background cell size is maintained outside of the refinement boxes, specifically $5H_{ref}$ higher and $10H_{ref}$ downstream of the building. Depending on the grid resolution, the time step size is such that the maximum CFL number is lower than 1.0. A comparison of the pressure coefficient statistics obtained with all three meshes for the mean wind direction is included in Appendix A, showing that no significant changes were observed between the baseline and the fine cases for all QoIs. The root-mean-square errors between the fine and baseline mesh were 0.014 for C_p^{mean}, 0.005 for C_p^{rms}, 0.078 for C_p^{skew} and 0.42 for C_p^{kurt}. Thus, the baseline mesh resolution was used for all simulations reported in this paper. The time step for the baseline case is 10^{-4} s, which corresponds to a sampling frequency of 10,000 Hz.

3.4. Calculation of statistics

The statistics of the QoIs are estimated using 120 s of time series data for both the velocity and the pressure. This duration is the same as the WoW experiments and corresponds to 1846 τ_{ref}^{WoW}, where τ_{ref}^{WoW} is the flow-through time for the building based on the ratio of the building width and the speed at H_{ref}, i.e. $W_{ref}^{WoW}/U_{ref}^{WoW} = 1/15.2 \approx 0.066$ s. The time series were obtained after an initial burn-in period of at least 100 τ_{ref}. Regarding the UF experiments, the QoIs are estimated using 180 s, which corresponds to a non-dimensional time $\tau_{ref}^{UF} = W_{ref}^{UF}/U_{ref}^{UF} = 1/11.8 \approx 0.091$ s, and total duration of 1978 τ_{ref}^{UF}, which is similar to WoW.

4. Results and discussion

4.1. Comparison of ABL velocity statistics

In this section, the target experimental ABL velocity measurements are compared to the *WF* and *WF+RE* LES simulations in terms of mean velocity, turbulence intensities, length scales, and velocity spectra. For all simulations reported it was verified that spurious pressure fluctuations, which can occur when imposing a turbulent velocity field that is not strictly divergence-free (Patruno and de Miranda, 2020), were less than 0.05 C_p^{rms} at the intended building location.

4.1.1. Comparison of mean velocity and turbulence intensities

Fig. 7 compares the experimental non-dimensionalized mean velocity and the three turbulent intensities to the LES profiles. The WoW dashed lines represent the spanwise average at the center of the turntable, while the confidence intervals represent the minimum

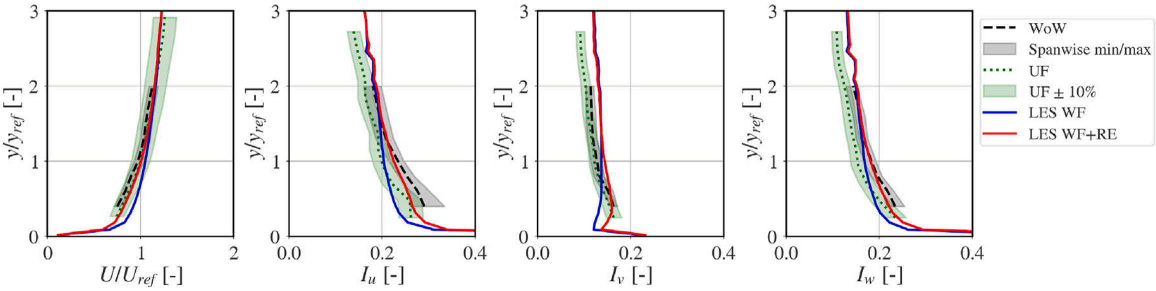

Fig. 7. Comparison of mean velocity and turbulence intensity between WoW, UF, LES rough, and LES smooth data.

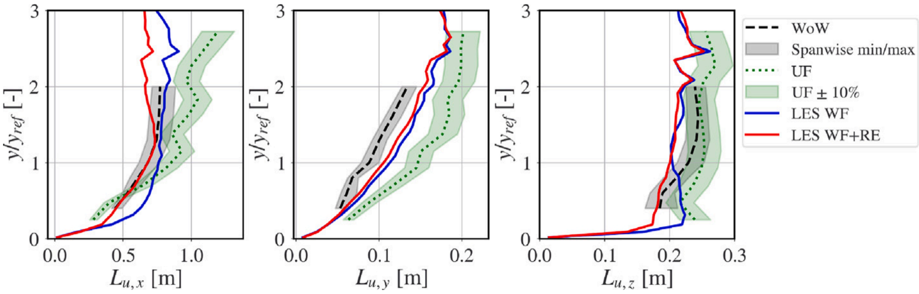

Fig. 8. Comparison of length scales between WoW, UF, LES rough, and LES smooth data.

and maximum values derived from various spanwise locations. The UF dashed line represents the profiles at the center of the turntable, while the confidence interval is set to $\pm 10\%$, which is similar to the WoW confidence intervals. All the LES profiles were obtained at the center of the turntable due to the spanwise uniformity observed in the time-averaged LES velocity statistics.

Fig. 7 shows that the *LES WF* underestimates the turbulence intensity at $y/y_{ref} < 1$ even though the inflow generator was used in conjunction with the gradient-based optimization. The building is inside this part of the ABL, which represents the roughness sublayer, and it is highly affected by the upstream roughness elements. To replicate the experimental profiles accurately, 10 rows of roughness elements are incorporated into the model. It is worth noting that when these roughness elements are omitted, the mean wind speed also accelerates due to the reduced upstream roughness. Consequently, this leads to discrepancies in the lower sections of the profiles. The addition of the roughness elements significantly improves the mean wind speed and all turbulent intensities at $y/y_{ref} < 1$. The *LES WF+RE* matches the experimental profiles at building height, and the discrepancies observed between the experiments and the LES are of the same order of magnitude as the discrepancies between the two experiments. This underscores the significance of explicitly resolving upstream roughness elements when modeling low-rise buildings.

4.1.2. Comparison of turbulence length scales

Fig. 8 compares the experimental length scales to those obtained by the LES. The introduction of the roughness elements in the simulation has a significant impact on the streamwise length scale, denoted as $L_{u,x}$, and the spanwise length scale, represented as $L_{w,x}$, while the vertical length scale, denoted as $L_{v,x}$, remains unchanged.

Specifically, in the case of the *LES WF+RE* simulation, the streamwise length scale closely follows the experimental profiles for $y/y_{ref} < 1$, whereas the spanwise length scale is slightly underestimated. Notably, the vertical length scale is between the profiles generated by the WoW and UF.

4.1.3. Comparison of velocity spectra

Fig. 9 shows the streamwise velocity spectra at the building height, including a comparison to the von Karman spectrum. The spectra were calculated using the Welch method (Welch, 1967). The four profiles consistently agree up to the minimum non-dimensional frequency that can be resolved by the LES. The WoW results include higher nondimensional frequencies than the UF results since a higher non-dimensional sampling frequency was used. The consistent agreement with the von Karman spectra indicates that the turbulence generated in the LESs and the experiments has a realistic energy distribution across the turbulence spectrum. In combination with the good agreement in the time-averaged velocity, turbulence intensity, and length scale profiles, this result indicates that the *LES WF+RE* has a very similar incoming ABL as the WoW and UF experimental set-ups. Consequently, this simulation setup is used for validating wind pressure predictions on the building in the next section.

4.2. Comparison of surface pressure statistics

In this section, the surface pressure statistics obtained from the WoW and UF experiments are compared to the LES results. The comparison is conducted in terms of contour plots, line plots, spectra, and correlation coefficients for the dominant wind direction. For a broader assessment of the predictive performance of the simulation, we also present scatterplots that compare the two experimental data sets and the LES results for four wind directions, spaced at intervals of 90° from the dominant wind direction. For all comparisons in this section, the WoW data will be considered the baseline dataset.

4.2.1. Contour plots on the building surface for the dominant wind direction

For better interpretability of the pressure loads on the building, Fig. 10 shows contour plots of the non-dimensional velocity magnitude around the building. Fig. 10(a) shows the ratio of the local velocity magnitude and velocity magnitude at the same height, at 0.02 m, while Fig. 10(b) and (c) the ratio of the local velocity magnitude and the reference velocity at 0.2 m. The dashed lines in Fig. 10(a) show the plane locations of Fig. 10(b) and (c). The contour plots of the normalized velocity show the complexity that governs this specific geometry.

Fig. 11 illustrates the spatial distribution of all QoIs across the building surface. The contour plots depicting the mean pressure coefficient (a1–a3) exhibit excellent qualitative agreement between the

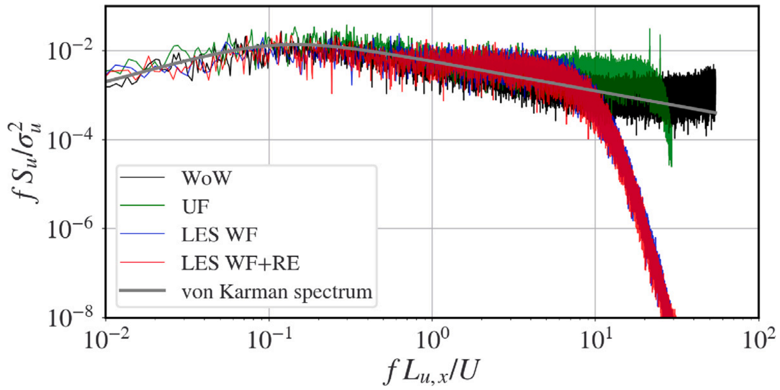

Fig. 9. Comparison of streamwise velocity spectra between WoW, UF, LES smooth, and LES rough data at 0.2 m height, compared to the Von Karman spectrum.

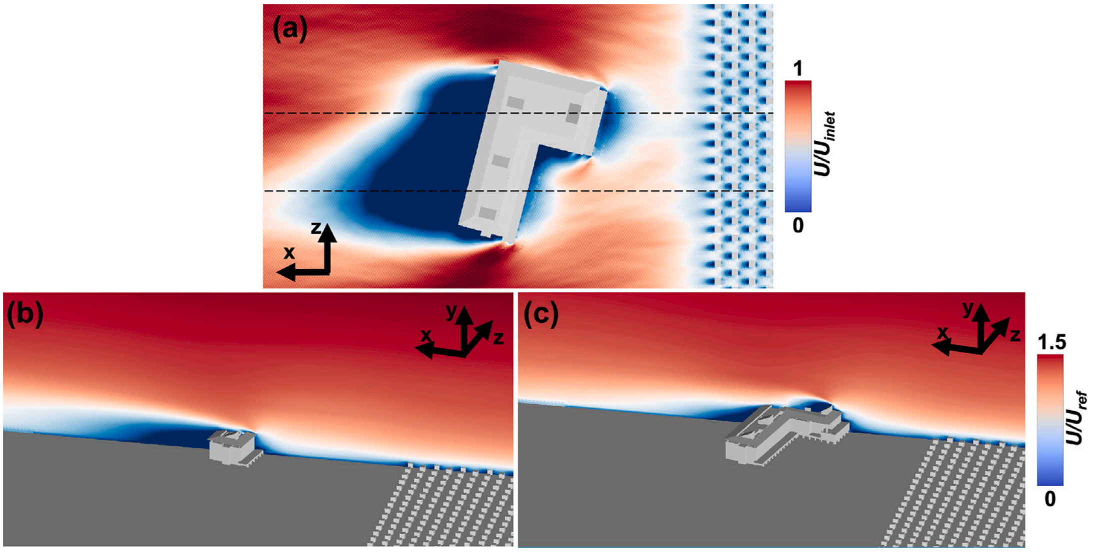

Fig. 10. Contour plots of the non-dimensional velocity magnitude on planes around the isolated building; (a): top view of the ratio between the local velocity magnitude and velocity magnitude at the inlet, at the same height (0.02 m), (b) & (c): side views of the ratio between the local velocity magnitude and reference velocity at building height (0.2 m).

two experiments and the LES. Notably, a positive pressure coefficient area is present at the north façade, indicative of flow stagnation, while other faces exhibit separated flow regions and wakes, which generate negative pressure coefficients. The strongest negative mean pressure coefficients appear on the left upstream side of the roof.

The contour plots of the rms pressure coefficients (b1–b3) reveal a similar excellent qualitative agreement between the experiments and the LES. On the north façade, where the flow stagnates, rms values between 0.2 and 0.4 are observed, and the LES values are slightly higher than the experimental data. The highest rms values occur in the region on the roof that has the most negative mean pressure coefficient values, indicating significant turbulent fluctuations in the flow.

Qualitative agreement is also maintained in the peak pressure coefficient distribution (c1–c3). As expected from the mean and rms pressure coefficients, the most negative values occur on the left upstream part of the roof. Across most of the roof, the LES appears to provide slightly more negative estimates of the peak suction values than the experiments. The two side façades have additional regions with low peak pressure coefficients in both experiments and the LES.

Contour plots of the skewness (d1–d3) and excess kurtosis (e1–e3) further reveal consistent predictions. Skewness is positive in the stagnated flow region on the north façade and negative in regions with strong flow separation. The skewness values in the UF and LES data are higher than the WoW data in a few regions of the flow, most notably on the north, east, and downstream parts of the west façade. The excess kurtosis is locally highest in a few select locations on the building roof, which indicates the occurrence of occasional strong negative pressure peaks. Overall, the kurtosis values tend to be slightly higher in the LES, which explains the higher estimates for the peak pressure coefficients. The most pronounced differences appear on upstream façades where the wind impacts on the envelope, indicating that differences in the incoming wind field might have an effect. The most pronounced difference observed in the wind flow conditions generated in the empty wind tunnels and LES domains was in the vertical turbulence length scales (see Fig. 8). Additional analysis also revealed some differences in the skewness and excess kurtosis in the wind velocity time series. In particular, the skewness and excess kurtosis of the u velocity component were approximately two times higher in the LES as opposed to the experimental data. An in-depth analysis of the dependency of the skewness and kurtosis of the pressure signal on the turbulence length scales and higher-order statistics of the incoming wind field is outside of the scope of this paper, but it is an interesting area for future research.

4.2.2. *Line plots on the building surface for the dominant wind direction*

To provide a detailed quantitative comparison, Fig. 12 provides line plots of the QoIs along three rows of taps at different heights:

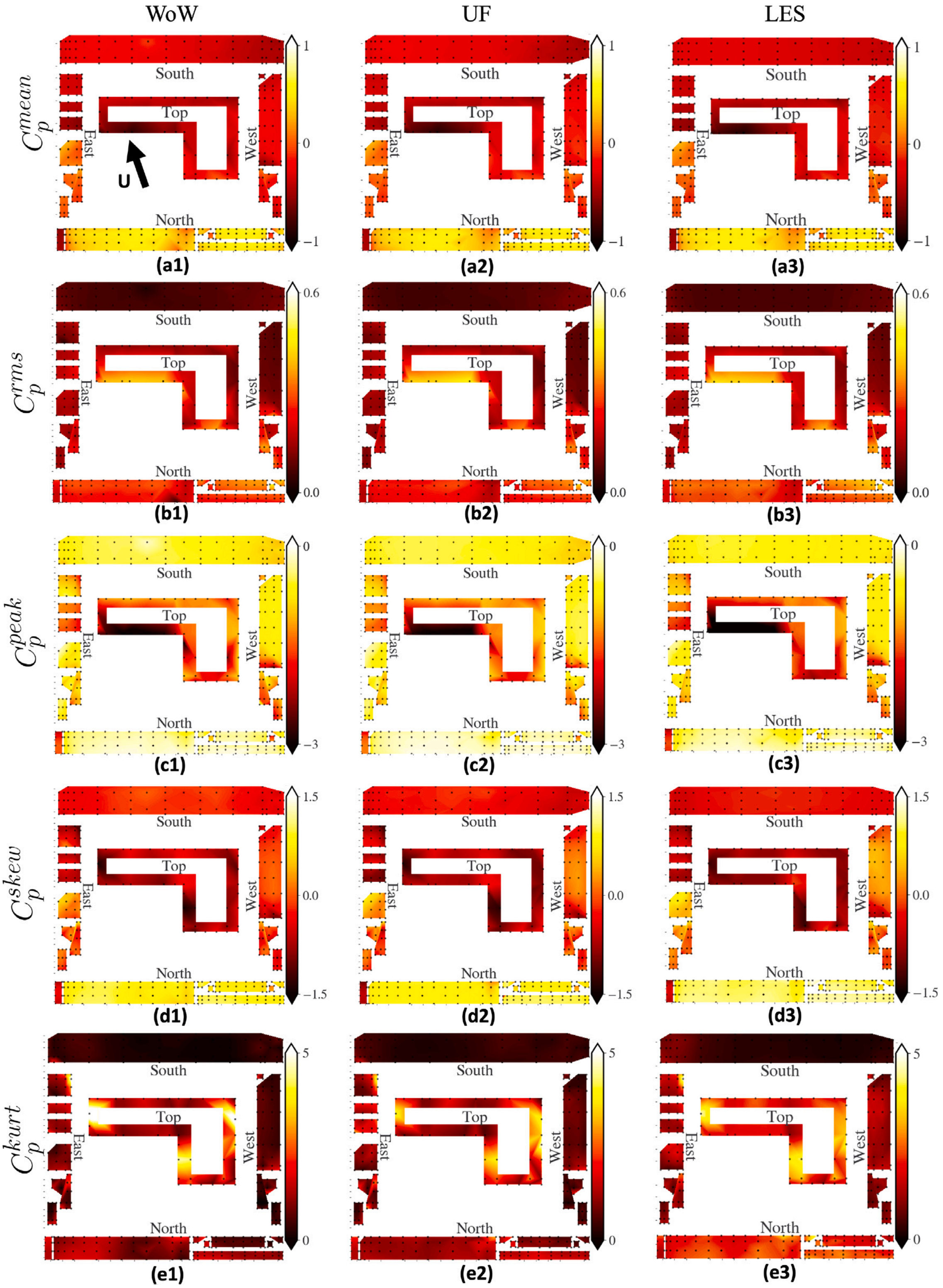

Fig. 11. Contour plot comparison of mean, rms, peak, skewness, and excess kurtosis of pressure coefficient for the WoW, UF, and LES data. All plots correspond to the most dominant wind direction. The north façade corresponds to flow stagnation, while other faces exhibit separated flow regions and wakes.

$y/y_{ref} = 1/3,\ 2/3\ \&\ 1$. The experimental data include a representation of the uncertainty related to the spanwise variation in the mean velocity profile across the width of the building. The profiles confirm the good agreement between the two experiments and the LES observed in the contour plots. Both UF and LES fall within the WoW confidence intervals at almost every tap location for the mean, rms, and peak pressure coefficient values. The skewness also predominantly falls within the WoW error bars, with the difference between WoW and LES not surpassing ±0.1. Similarly, the excess kurtosis difference between WoW and LES remains below ±1.2. Interestingly, there is consistency in the locations where discrepancies occur, i.e. the regions where the UF data deviates from the WoW data are also the regions where there

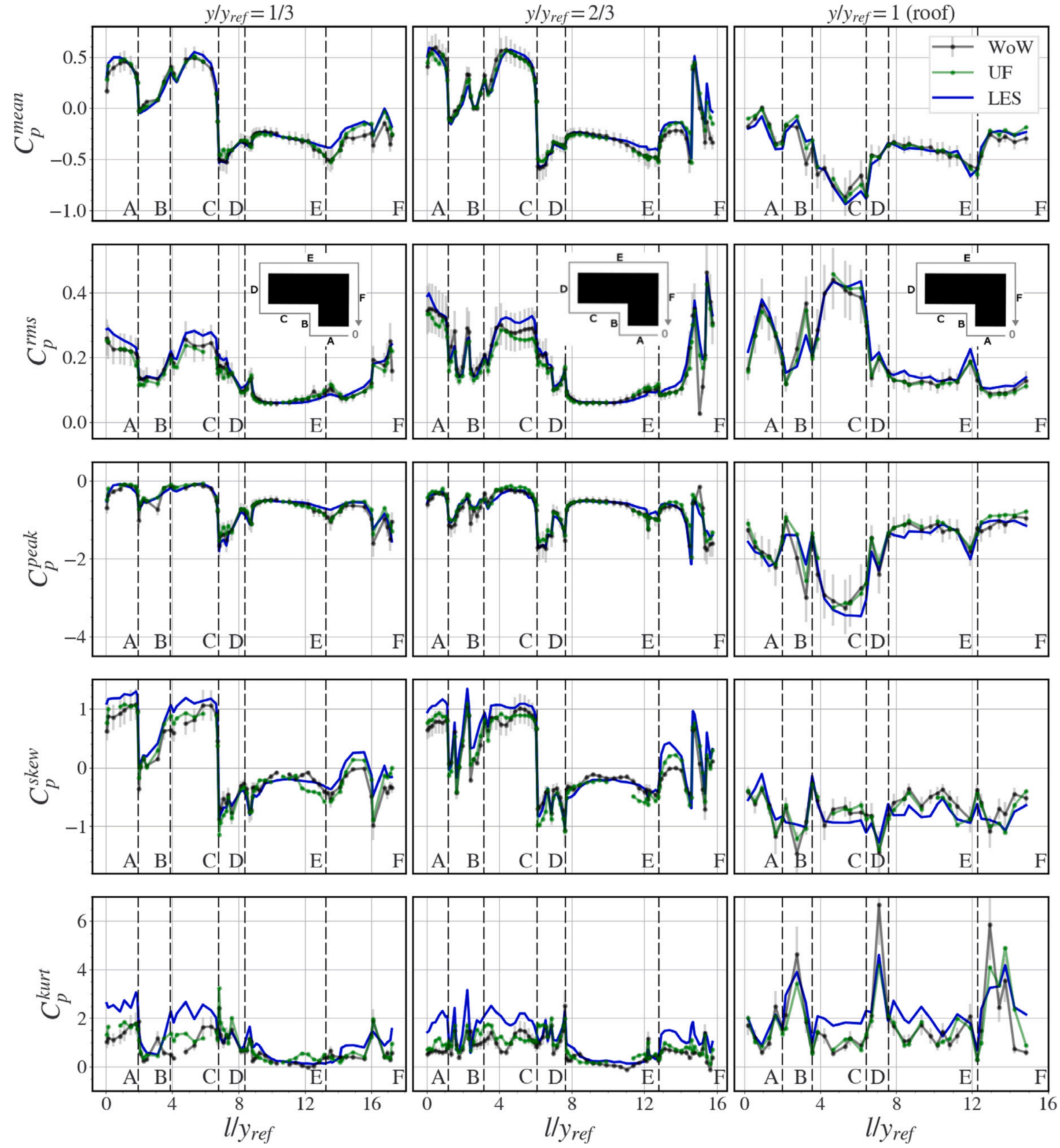

Fig. 12. Line plots comparison of mean, rms, peak, skewness, and excess kurtosis of pressure coefficient for the WoW, UF, and LES data at the perimeter of the building. All plots correspond to the most dominant wind direction.

are discrepancies with the LES data. As noted in the discussion of the contour plots, these locations are primarily on upstream façades, where the wind flow impacts on the envelope. This observation further supports the hypothesis that the higher-order moments of the pressure time series might be affected by the turbulence length scales and higher-order moments in the incoming wind field.

4.2.3. Comparison of pressure coefficient statistics for four wind directions

For a broader assessment of the predictive capabilities of the LES model and the two wind tunnel experiments, a comparative analysis is conducted for four different wind directions at intervals of 90°. Fig. 13 presents the error plots of the C_p statistics. The scatter plots show the QoIs for all the taps across various wind directions, overlaid with ±10%, ±20%, and ±30% error margins. Accompanying the scatter plots are error bars that depict the average error across all directions for each pair of WoW, UF, and LES. The errors for all QoIs are presented as direct differences ($RMSE$). The $RMSE$ is defined as follows:

$$RMSE = \sqrt{\frac{\sum_{k=1}^{N}(r^{M1}(x_k) - r^{M2}(x_k))^2}{N}}. \tag{9}$$

N is the number of taps, r is the quantity of interest, x_k is the tap location, and $M1$ and $M2$ are the methods to compare.

The agreement among C_p^{mean} values for all methods is generally very good, with $RMSE$ less than 0.1 across all façades as depicted by the error bars in Fig. 13. An important observation is that the $RMSE$ of the two experiments $WoW - UF$ (solid error bar), particularly at the north façade, is higher than the $RMSE$ between $WoW - LES$ (single-dashed error bars) and $UF - LES$ (double-dashed error bars). Essentially, this suggests that the error between the two experiments is higher compared to the errors between LES and each experiment individually. A similar

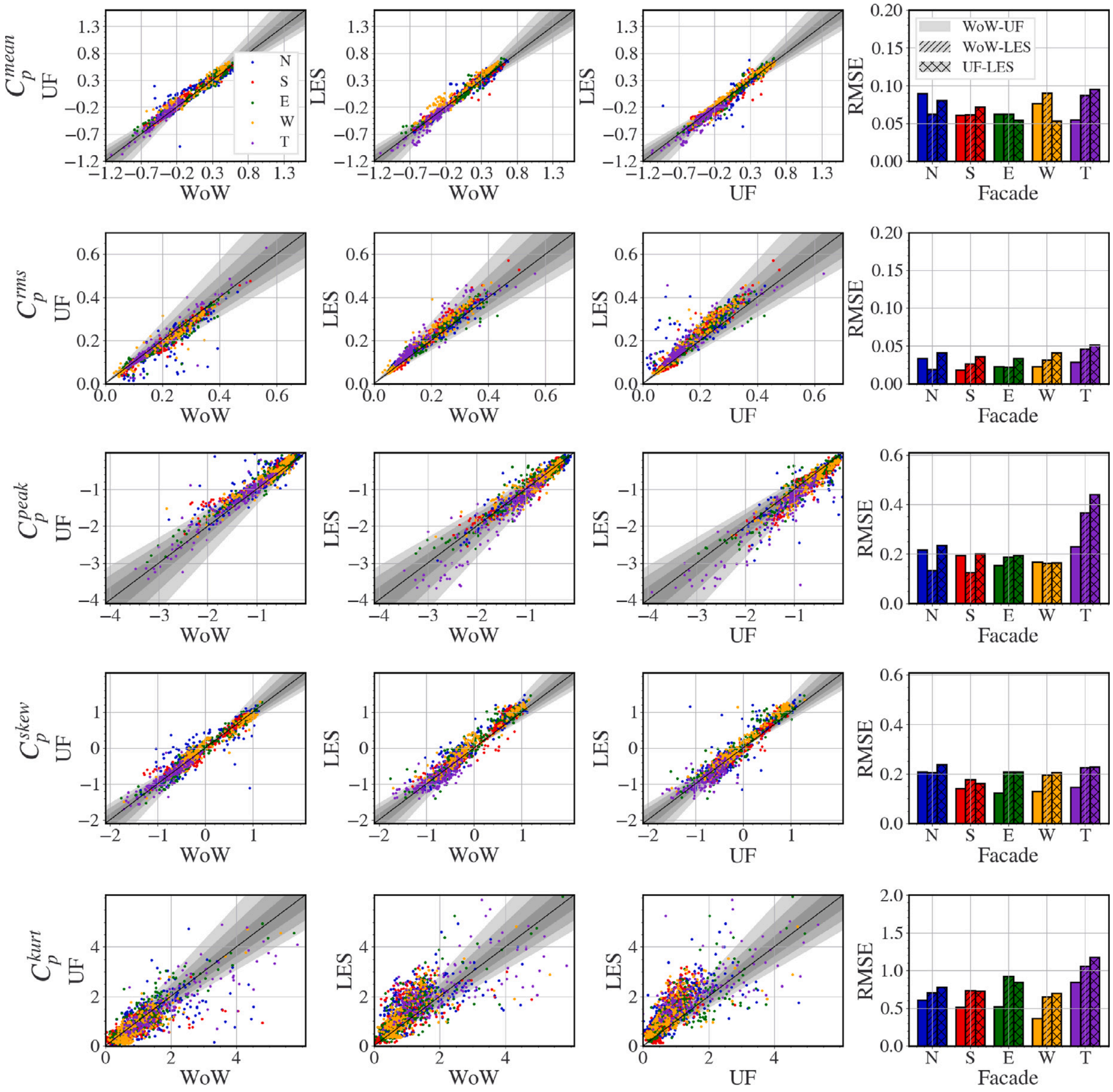

Fig. 13. Comparison of mean, rms, peak, skewness, and excess kurtosis between all pairs of WoW-UF-LES, for all four wind directions. Left: scatter plots and Right: quantified error given by $RMSE$. Gray shaded area corresponds to 10%, 20%, and 30% error.

trend is evident on the east side of the building. Conversely, when considering the top face, $WoW - UF$ exhibits the lowest error.

For C_p^{rms}, the agreement is maintained within $RMSE$ of 0.05 across all faces. Notably, the scatterplots show that $WoW - LES$ displays the fewest outliers. Moreover, $WoW - UF$ and $UF - LES$ exhibit discrepancies at the same tap locations, marked by the numerous blue (north) outliers and some yellow (west) outliers. This observation aligns with the $RMSE$ values for these faces. Regarding the top face, $WoW - UF$ once again, shows the lowest error.

Similarly, C_p^{peak} shows a comparable trend to C_p^{rms} with $RMSE$ values less than 0.2 on most of the faces. $WoW - LES$ records the lowest value on the north and south faces. This can also be confirmed by the scatter plots, where $WoW - UF$ and $UF - LES$ show numerous blue (north) and red (south) outliers.

Concerning C_p^{Skew} and C_p^{Kurt}, the $RMSE$ between the compared datasets remain less than 0.2 and 1, respectively, for most faces. The $WoW - UF$ $RMSE$ is slightly lower for all faces compared to $WoW - LES$ and $UF - LES$, which show a higher spread in the scatter plots. This concurs with the line plots in Fig. 12, where LES predictions were marginally higher.

Although LES model predictions for C_p^{Skew} and C_p^{Kurt} are slightly higher, the overall performance closely aligns with the two experiments. It is noteworthy that when the mean, rms, and peak C_p are considered, the error for $WoW - UF$ is comparable to $WoW - LES$ and $UF - LES$. Most importantly, when comparing the two experiments, they exhibit discrepancies in the same locations as LES. In summary, the comparison in this section showed that a carefully designed LES can accurately predict not only the mean, rms, and peak C_p but also higher-order statistics such as skewness and excess kurtosis.

4.3. Time series analysis at three points on the building surface

In this section, a closer examination of the results at three taps on the building, as shown in Fig. 14, is presented. The analysis includes plots of the time history, non-dimensional C_p spectra, probability density function (PDF), and auto-correlation coefficients. The auto-correlation coefficient is given by:

$$\rho(\tau) = \frac{E[(C_p(t) - C_p^{mean})(C_p(t+\tau) - C_p^{mean})]}{E[(C_p(t) - C_p^{mean})^2]}, \quad (10)$$

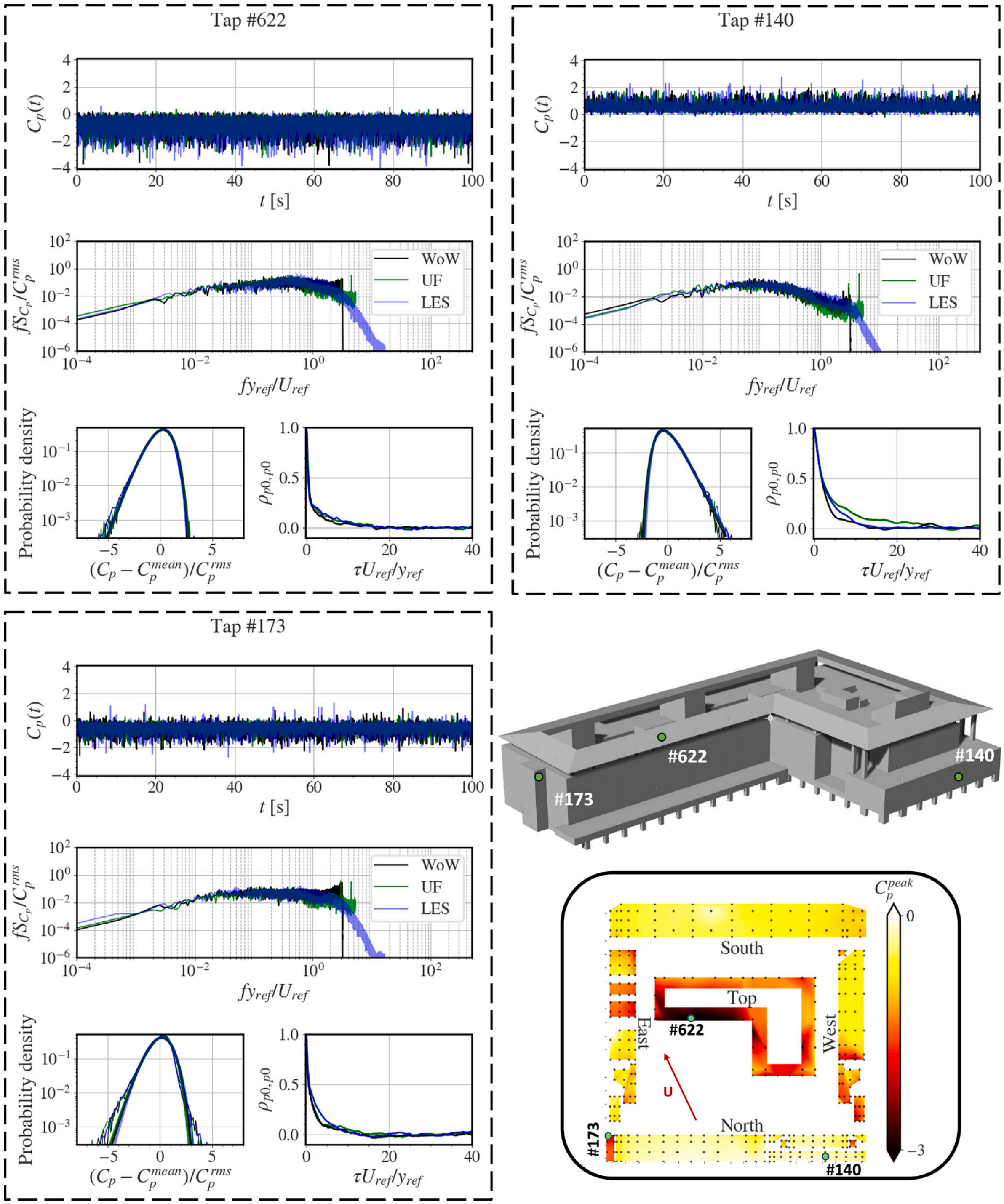

Fig. 14. Comparison of C_p time series, pressure spectra, probability density function, and auto-correlation coefficient plots between the WoW, UF, and LES data at selected tap locations. All plots correspond to the most dominant wind direction.

where E is the expected value of the square brackets. The selection of the three taps is based on areas of interest where the pressure coefficient exhibits substantial negative or positive values. Taps #173 and #622 correspond to separated flow regions, while tap #140 is in a stagnated flow region.

Considering the C_p time series, the LES solution and the two experiments provide a very similar range of values at the three taps considered. In all cases, taps #622 and #173 show significant skewness towards negative values, while tap #140 skews towards positive values. The C_p spectra confirm that the LES is in close agreement with the two experiments across a broad frequency range for all taps. This behavior is consistently observed across all locations on the building.

The skewness of the C_p signal is confirmed by the PDFs included in Fig. 14. For taps #173 and #622 the tails extend towards strong negative values, while tap #140 exhibits stronger positive peaks. The PDFs can be approximated by log-normal fits and the fits agree well between the LES and both experiments. The negative skewness and high kurtosis of the C_p signal in separation regions has been previously observed in both experimental studies and CFD simulations. The tails of the LES signals are slightly heavier than those of the two experiments, which

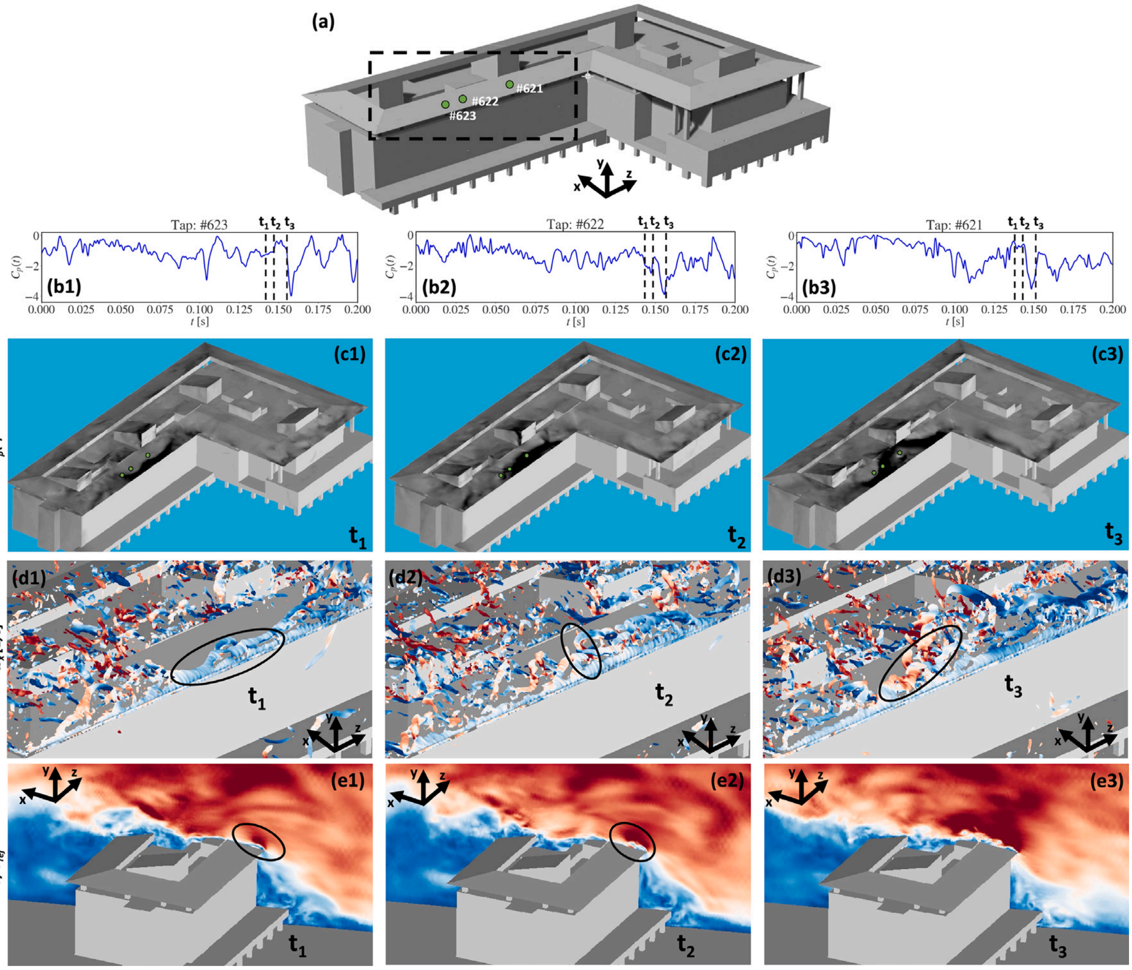

Fig. 15. (a): Building geometry with the area of focus indicated by the dashed rectangle and the tap locations shown in green. The freestream wind is aligned with the x-direction. (b) Time series of the pressure coefficient at taps #623, #622, and #621. (c) Instantaneous pressure coefficient contours on the building surface. (d) Iso-surfaces of Q criterion colored by x-vorticity at three different times. (e) Contour plots of the normalized wind magnitude U/U_{ref} on a plane through tap #621 and aligned with the freestream wind direction.

corresponds to the higher values of the C_p peak and excess kurtosis presented previously.

The autocorrelation plots included in Fig. 14 agree well between the LES and the two experiments in the separated flow regions at taps #622 and #173. However, the auto-correlation at tap #140, which corresponds to a stagnated flow regions, shows a faster decay in the WOW experiment compared to the UF experiment. The LES decay rate lies between the two experiments. A plausible explanation for this trend is the difference in the turbulent length scales $L_{u,y}$ in the incoming wind field (see Fig. 8), with the WoW showing the smallest length scales, and the UF the largest.

4.4. Flow visualization of a single pressure peak

To improve our qualitative understanding of the flow phenomena responsible for the strong negative pressure peak events on the roof, Fig. 15 presents additional flow visualization results, similar to visualizations performed in previous experimental and computational studies (Saathoff and Melbourne, 1997; Ciarlatani et al., 2023). The focus is on a specific peak event observed at the roof of the building. The flow direction is aligned with the x direction and the region of interest is highlighted by the dashed box in Fig. 15(a). Time series data collected at taps #621, #622, and #623 are presented in (b1–b3). The plots include three time stamps right before and during the occurrence of a large pressure drop (C_p around -4) at the three taps. The remaining rows in the figure include contours of the instantaneous pressure coefficient (c1–c3), iso-surfaces of the Q criterion (Hunt et al., 1988) colored by streamwise vorticity (d1–d3), and contours of the normalized velocity magnitude U/U_{ref} (e1-e3) at these three time instances. The plane on which the normalized magnitude U/U_{ref} is shown is aligned with the wind direction and located at tap #621.

At time t1, the contours in (c1) indicate that the flow is characterized by a separated flow region with low pressure that spans across most of the width of the upstream edge of the building roof. This low pressure region is paired with the presence of a long vortex, highlighted in the plot of the iso-surface of the Q criterion in (d1). Figure (e1) shows that this structure is paired with a small localized region of high velocity. From this vortex shown at t1, hairpin-like vortices are formed and lifted at time t2. The tail of one of these vortices is highlighted with the black oval in (d2), while the enlarged high velocity region is indicated in (e2). The tail of the lifted vortex stays close to the surface and causes a large negative peak pressure when it passes over tap #621 at t_2. Later, at time t_3, the high-velocity region above the roof has increased even further in size, as shown in (e3). This high velocity region is paired with further stretching and formation of vortices, as shown in the black oval (d3), and the combination of the strength of these vortices and their proximity to the surface causes strong negative pressures over a significant portion of the roof with local peaks at pressure taps #622, and #623. This mechanism of creating a strongly correlated vortex across the width of the roof from which hairpin-like vortices are lifted and advected across the roof happens repeatedly, resulting in the large negative peak pressure coefficients observed in this location.

5. Conclusions

The experiments and simulations presented in this paper have been used for successful validation of an LES workflow for predicting wind loading on a realistic low-rise building geometry. Pressure measurements were conducted on a 1:100 scale model of Stanford's Y2E2 building exposed to a suburban neutral surface layer flow in two different wind tunnels: the NHERI Wall of Wind (WoW) open-circuit wind tunnel at Florida International University and the NHERI terraformer (UF) Boundary Layer Wind Tunnel at the University of Florida. LESs were performed using the CharLES code. In both experiments and simulations a two-step workflow was followed.

First, we ensured that an accurate representation of the surface layer wind flow in terms of the profiles of mean velocity, turbulence intensities, and turbulence length scales was obtained. These profiles were characterized by performing measurements and simulations of the flow in the wind tunnel or numerical domain without the building model present, and by sampling the flow at the intended building location. In the wind tunnels, obtaining the target profiles required: (1) upstream spires, (2) roughness elements in the flow development section, and (3) additional roughness elements on the turntable. In the LESs, the equivalent setup consisted of: (1) a digital filter method to create a turbulent velocity field at the inflow, with the inputs optimized to obtain the target velocity statistics at the downtream location, (2) a wall function that supports a flow with the target roughness height, and (3) explicit representation of several (∼10) rows of roughness elements upstream of the building. The extension of the roughness elements onto the turntable and their equivalent inclusion in the LES model was found to be essential for accurate reproduction of the flow in the roughness sublayer. This is particularly important when modeling low-rise buildings that are immersed in this sublayer.

Subsequently, using the setups that correctly reproduced the surface layer flow, measurements and simulations that included the Y2E2 model were performed to obtain predictions for the mean, rms, peak, skewness, and excess kurtosis of the pressure coefficient C_p on the building surface.

The results for the mean, rms, and peak C_p showed excellent agreement between the LES and the two experiments. RMSE values between both experiments and the LESs are less than 0.1 and 0.05 across the entire building for the mean and rms C_p, respectively. For the peak C_p estimates, the RMSE values are around 0.2 on the facades. On the roof the RMSE between both experiments is 0.2, but the LES tends to predict more negative peak values than the experiments with an RMSE of around 0.4. The difference in the estimated peak values is related to the higher skewness and excess kurtosis of the pressure signals in the LESs compared to the experiments. It is noted that the observed discrepancies in these higher-order statistics remain within the uncertainty in the C_p values related to spanwise variability in the wind tunnel boundary layers.

Lastly, flow visualization using iso-surfaces of Q criteria was used to understand the flow phenomena responsible for the pressure peak events on the roof of the building. The iso-surfaces indicate a repeating process consisting of (1) the formation of a large vortex across the width of the roof, (2) the lifting of smaller hairpin-like vortices from this larger vortex, and (3) the tails of the vortices remaining close to the surface and causing the strongly negative pressure peaks.

To conclude, this research demonstrates that LES, when designed carefully, can be an accurate and reliable tool in predicting wind-induced pressure loads on realistic low-rise building models. The observed discrepancies between LES and wind tunnel data mirror the discrepancies between wind tunnel tests conducted at different facilities. Future research will explore two directions. First, we will investigate modeling the wind pressure loads on the same building but placed inside its urban area. This analysis will support further validation of LES for the calculation of wind loads in the presence of interference effects from surrounding buildings. Second, we aim to explore the validation of LES predictions at a larger scale, either by comparing to larger-scale experiments, or by comparing to field measurements. This analysis will support investigating the effects of the reduced Reynolds number or the absence of larger-scale, low-frequency velocity fluctuations in the small-scale experiments on the peak pressure coefficients. Ultimately, we aim to bridge the gap between wind tunnel experiments, field measurements, and computational approaches, making progress towards the widespread integration of CFD for wind load calculations and building design.

CRediT authorship contribution statement

Themistoklis Vargiemezis: Writing – review & editing, Writing – original draft, Visualization, Validation, Software, Methodology, Investigation, Formal analysis, Data curation. **Catherine Gorlé:** Writing – review & editing, Supervision, Methodology, Funding acquisition, Formal analysis, Conceptualization.

Declaration of competing interest

The authors declare that they have no known competing financial interests or personal relationships that could have appeared to influence the work reported in this paper.

Acknowledgments

This material is based upon work supported by the National Science Foundation, United States under Grant Number 1749610 and used the Extreme Science and Engineering Discovery Environment (XSEDE), which is supported by National Science Foundation, United States grant number CI-1548562. The NSF NHERI Experimental Facility of UF that contributed to the research results reported within this paper was supported under the grant number 2037725. We gratefully acknowledge our collaborators at the International University of Florida, James Erwin, Arindam Gan Chowdhury, Dejiang Chen, and Walter Conklin for conducting the WoW experiments. We also acknowledge our collaborators at the University of Florida, Jennifer Bridge, Ryan Catarelli, and Scott Powell for conducting the UF experiments.

Appendix A. Grid dependency results

Fig. A.16 presents the comparison of the line plots of the mean, rms, peak, skewness, and excess kurtosis values of the pressure coefficient for the three different grid resolutions reported in Table 5. The plots confirm that the differences between the baseline and fine mesh are negligibly small across all pressure taps.

Data availability

The WoW and UF experimental datasets are available to the scientific community on the NSF NHERI DESIGNSAFE repository (Vargiemezis and Gorle, 2024).

References

Alrawashdeh, H., Stathopoulos, T., 2015. Wind pressures on large roofs of low buildings and wind codes and standards. J. Wind Eng. Ind. Aerodyn. 147, 212–225.

Ambo, K., Nagaoka, H., Philips, D.A., Ivey, C., Brès, G.A., Bose, S.T., 2020. Aerodynamic force prediction of the laminar to turbulent flow transition around the front bumper of the vehicle using dynamic-slip wall model LES. In: AIAA Scitech 2020 Forum. p. 0036.

ASCE, A.S.o.C.E., 2022. Minimum Design Loads and Associated Criteria for Buildings and Other Structures, ASCE/SEI 7-22. American Society of Civil Engineers.

Blocken, B., 2014. 50 years of computational wind engineering: past, present and future. J. Wind Eng. Ind. Aerodyn. 129, 69–102.

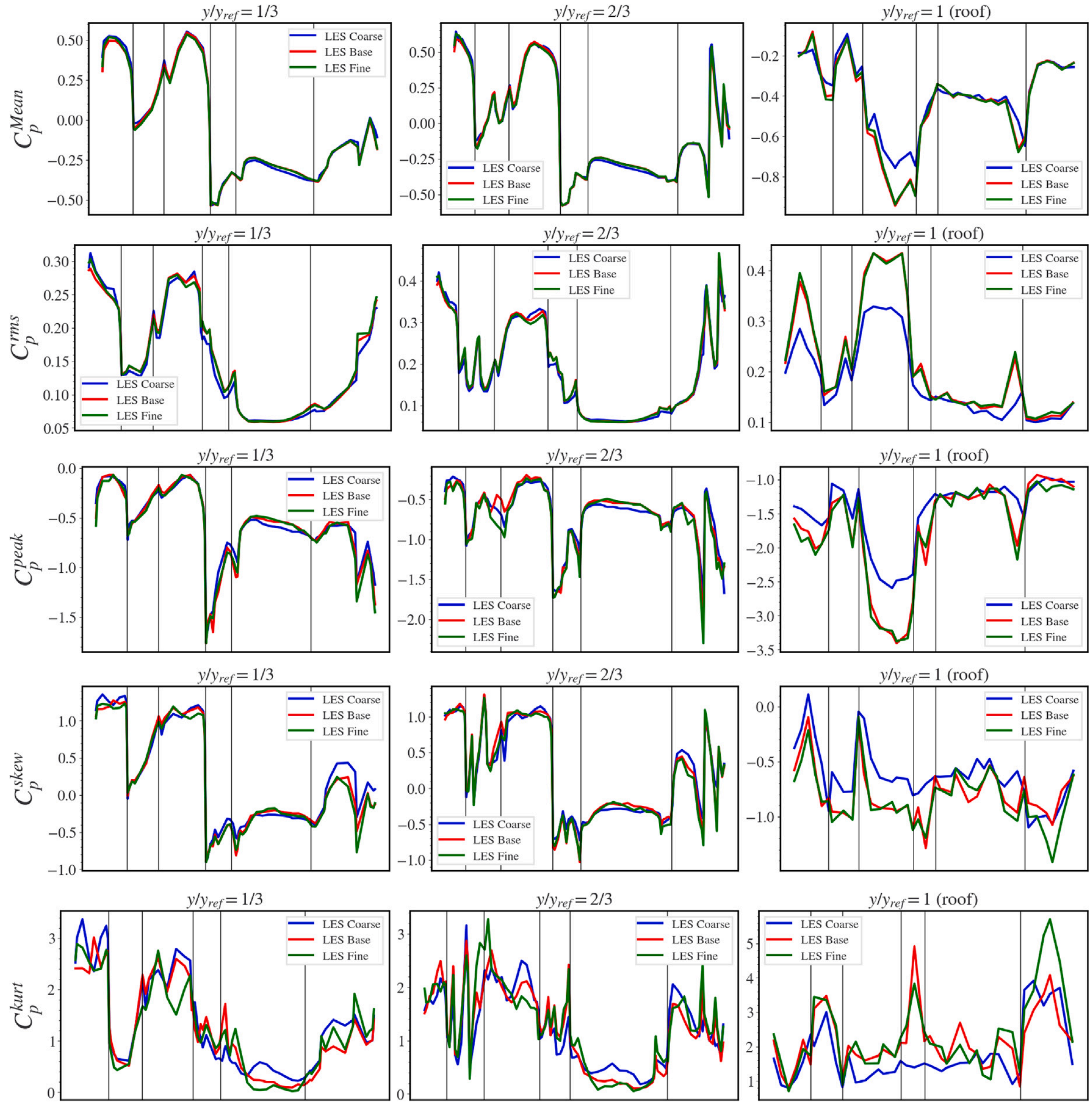

Fig. A.16. Comparison of line plots of the mean, rms, peak, skewness, and excess kurtosis of the pressure coefficient for different grid resolutions. All plots correspond to the dominant wind direction.

Catarelli, R.A., Fernández-Cabán, P.L., Phillips, B.M., Bridge, J.A., Masters, F.J., Gurley, K.R., Prevatt, D.O., 2020. Automation and new capabilities in the university of florida NHERI boundary layer wind tunnel. Front. Built Environ. 6, 558151.

Ciarlatani, M.F., Huang, Z., Philips, D., Gorlé, C., 2023. Investigation of peak wind loading on a high-rise building in the atmospheric boundary layer using large-eddy simulations. J. Wind Eng. Ind. Aerodyn. 236, 105408.

Cook, N., Mayne, J., 1980. A refined working approach to the assessment of wind loads for equivalent static design. J. Wind Eng. Ind. Aerodyn. 6 (1–2), 125–137.

Franke, J., Hellsten, A., Schlunzen, K.H., Carissimo, B., 2011. The COST 732 best practice guideline for CFD simulation of flows in the urban environment: a summary. Int. J. Environ. Pollut. 44 (1–4), 419–427.

Gan Chowdhury, A., Zisis, I., Irwin, P., Bitsuamlak, G., Pinelli, J.-P., Hajra, B., Moravej, M., 2017. Large-scale experimentation using the 12-fan wall of wind to assess and mitigate hurricane wind and rain impacts on buildings and infrastructure systems. J. Struct. Eng. 143 (7), 04017053.

Geleta, T.N., Bitsuamlak, G., 2022. Validation metrics and turbulence frequency limits for LES-based wind load evaluation for low-rise buildings. J. Wind Eng. Ind. Aerodyn. 231, 105210.

Holmes, J., 1983. Wind Loads on Low Rise Buildings: A Review. Commonwealth Scientific and Industrial Research Organization, Division of Building Research, URL https://books.google.com/books?id=otk0twAACAAJ.

Hunt, J.C., Wray, A.A., Moin, P., 1988. Eddies, streams, and convergence zones in turbulent flows. In: Studying Turbulence Using Numerical Simulation Databases, 2. Proceedings of the 1988 Summer Program.

Hwang, Y., Gorlé, C., 2022. Large-eddy simulations of wind-driven cross ventilation, Part1: validation and sensitivity study. arXiv preprint arXiv:2204.00786.

Hwang, Y., Gorlé, C., 2023. Large-eddy simulations to define building-specific similarity relationships for natural ventilation flow rates. Flow 3, E10.

Kasperski, M., 1996. Design wind loads for low-rise buildings: A critical review of wind load specifications for industrial buildings. J. Wind Eng. Ind. Aerodyn. 61 (2–3), 169–179.

Kim, Y., Castro, I.P., Xie, Z.-T., 2013. Divergence-free turbulence inflow conditions for large-eddy simulations with incompressible flow solvers. Comput. & Fluids 84, 56–68.

Lamberti, G., García-Sánchez, C., Sousa, J., Gorlé, C., 2018. Optimizing turbulent inflow conditions for large-eddy simulations of the atmospheric boundary layer. J. Wind Eng. Ind. Aerodyn. 177, 32–44.

Lamberti, G., Gorlé, C., 2020. Sensitivity of LES predictions of wind loading on a high-rise building to the inflow boundary condition. J. Wind Eng. Ind. Aerodyn. 206, 104370.

Patruno, L., de Miranda, S., 2020. Unsteady inflow conditions: A variationally based solution to the insurgence of pressure fluctuations. Comput. Methods Appl. Mech. Engrg. 363, 112894.

Ricci, M., Patruno, L., De Miranda, S., 2017. Wind loads and structural response: Benchmarking LES on a low-rise building. Eng. Struct. 144, 26–42.

Richards, P., Norris, S., 2015. LES modelling of unsteady flow around the silsoe cube. J. Wind Eng. Ind. Aerodyn. 144, 70–78.

Saathoff, P.J., Melbourne, W.H., 1997. Effects of free-stream turbulence on surface pressure fluctuations in a separation bubble. J. Fluid Mech. 337, 1–24.

Shao, S., Stathopoulos, T., Yang, Q., Tian, Y., 2018. Wind pressures on 4∶ 12−sloped hip roofs of L-and T-shaped low-rise buildings. J. Struct. Eng. 144 (7), 04018088.

Smith, A.B., 2023. NOAA national centers for environmental information (NCEI) U.S. billion-dollar weather and climate disasters (2023). https://www.ncei.noaa.gov/access/billions/. (Accessed 30 October 2023).

Stathopoulos, T., 1984. Wind loads on low-rise buildings: a review of the state of the art. Eng. Struct. 6 (2), 119–135.

Vargiemezis, T., Gorle, C., 2024. Wind tunnel experiments on realistic low-rise building in urban area. http://dx.doi.org/10.17603/DS2-5APM-V542, URL https://www.designsafe-ci.org/data/browser/public/designsafe.storage.published/PRJ-2571/#detail-4070145275427230191-242ac118-0001-012/?version=2.

Vreman, A., 2004. An eddy-viscosity subgrid-scale model for turbulent shear flow: Algebraic theory and applications. Phys. Fluids 16 (10), 3670–3681.

Welch, P., 1967. The use of fast Fourier transform for the estimation of power spectra: a method based on time averaging over short, modified periodograms. IEEE Trans. Audio Electroacoust. 15 (2), 70–73.